JMEPEG (2020) 29:776–786
https://doi.org/10.1007/s11665-020-04619-x

1059-9495/$19.00

Effects of Trace Ce Addition on Hot Deformation Behavior of Cu-0.8 Mg Alloy

Guoqiang Sun, Yong Liu, Baohong Tian, Yi Zhang, Zhengbin Gu, and Alex A. Volinsky

(Submitted December 13, 2018; in revised form January 13, 2020; published online February 10, 2020)

Hot deformation tests of Cu-0.8 Mg and Cu-0.8 Mg-0.15 Ce alloys were carried out with a Gleeble-1500D thermal simulator in the temperature range of 500-850°C and the strain rate range of 0.001-10 s^{-1}. Based on compression tests, flow stress–strain curves and processing maps of Cu-0.8 Mg and Cu-0.8 Mg-0.15 Ce alloys were plotted, and constitutive equations of the two alloys were constructed. The microstructure of the two alloys under different hot deformation conditions was observed and analyzed by optical microscopy. The trace addition of Ce restricted the movement of dislocations, promoted dynamic recrystallization, increased the flow stress and activation energy for hot deformation and enlarged the hot working region compared to the alloy without trace Ce addition.

Keywords constitutive model, Cu-0.8 Mg alloy, Cu-0.8 Mg-0.15 Ce alloy, hot deformation tests, processing maps

1. Introduction

Copper alloys are widely used in different industries, including electrical, electronics, machinery manufacturing, chemical, construction, national defense and many other industries due to their good conductivity, corrosion resistance, plasticity, formability and durability (Ref 1–4). With the rapid development of science and technology, copper alloys are used in many applications and the demands for these alloys are still growing. Due to low mining cost, good physical properties and abundant natural deposits, copper is considered as a new functional material with good applications potential and development prospects. At the same time, more stringent performance requirements are put forward for copper and its alloys. Researchers have also developed many new copper alloys, such as medium-strength and high-conductivity Cu-Fe-P alloy (Ref 5, 6), high-strength and medium-conductivity Cu-Ni-Si alloy (Ref 7, 8), high-strength and high-conductivity Cu-Cr-Zr alloy (Ref 9, 10) and so on. To improve the comprehensive properties of copper and its alloys, trace elements are often added at optimal concentration. For example, Si can assist in deoxidation purification and improve the fluidity of the alloys (Ref 11). Sn can inhibit the aging process of Mg (Ref 12). Dislocation pinning is improved by the precipitation of added Ce, and both mechanical and chemical properties of the alloy can be improved remarkably by adding P and Ce (Ref 13, 14). Cu-Mg is a multi-component copper alloy with high hardness and electrical conductivity, which is used in railway contact wires, tramlines, aircraft antennas and so on. Lots of scholars have performed research on Cu-Mg alloys, but special processing methods are needed to manufacture copper alloy with high strength and high conductivity. However, these methods are not yet suitable for commercial use. With the increasing speed of high-speed railways, the properties of contact wire materials also need to be improved. There are stricter requirements for materials, but less research has been done on the hot deformation of copper alloys with high Mg content. Zhang et al. (Ref 15) studied the hot deformation behavior of the Cu-Zr-Cr-Ce alloy and found that trace addition of Ce increases flow stress and promotes dynamic recrystallization of the alloy. Therefore, the addition of Ce may further improve the hot workability of the Cu-Mg alloy.

In this paper, hot deformation experiments with Cu-0.8 Mg and Cu-0.8 Mg-0.15 Ce alloys under different deformation conditions were carried out using a Gleeble-1500D thermal deformation simulator. Based on the data obtained from the two tested alloys, the flow stress–strain curves and the processing maps are plotted, and the constitutive equations are constructed. The microstructure of the two alloys under different hot deformation conditions is observed and analyzed by optical microscopy. These results provide reference for industrial production processes.

Guoqiang Sun, School of Material Science and Engineering, Henan University of Science and Technology, Luoyang 471023, China; **Yong Liu**, School of Material Science and Engineering, Henan University of Science and Technology, Luoyang 471023, China; Collaborative Innovation Center of Nonferrous Metals, Luoyang 471023 Henan Province, China; and Henan Key Laboratory of Advanced Non-Ferrous Materials, Luoyang 471023, China; **Baohong Tian**, School of Material Science and Engineering, Henan University of Science and Technology, Luoyang 471023, China; and Collaborative Innovation Center of Nonferrous Metals, Luoyang 471023 Henan Province, China; **Yi Zhang**, School of Material Science and Engineering, Henan University of Science and Technology, Luoyang 471023, China; and Henan Key Laboratory of Advanced Non-Ferrous Materials, Luoyang 471023, China; **Zhengbin Gu**, National Laboratory of Solid State Microstructures, Department of Materials Science and Engineering, College of Engineering and Applied Sciences, Nanjing University, Nanjing 210093, China; and **Alex A. Volinsky**, Department of Mechanical Engineering, University of South Florida, Tampa 33620. Contact e-mails: liuyong@haust.edu.cn and volinsky@usf.edu.

2. Experiment

The two alloys researched in this study were Cu-0.8 Mg and Cu-0.8 Mg-0.15 Ce. The 99.5 wt.% standard cathode copper, Mg with 99.5% purity and Ce with 99.5% purity were prepared and smelted in the ZG-0.01-40-4 vacuum furnace at 1200°C. After smelting, the alloys were cast into ingots with 80 mm diameter and 150 mm length. After casting, the ingots were extruded by the XJ-500 extruder into two bars with a diameter of 33 mm at 900°C. Then, the bars were heated to 900°C for 1 h before water quenching followed by machining into cylindrical specimens with 8 mm diameter and 12 mm length for hot compression tests, as shown in Fig. 1.

The hot compression tests of the Cu-Mg and Cu-Mg-Ce alloys were carried out using a Gleeble-1500D thermal simulator in a temperature range of 500-850°C and strain rate range of 0.001-10 s^{-1}. The total compression deformation of the specimens was about 55%. The specimens were heated to a specified deformation temperature at 10°C/s and held for 1 min before hot compression testing according to the schematic of hot deformation in Fig. 2. After hot deformation, the specimens were quenched in water to retain the high-temperature microstructure. Schematics of specimens' geometry before and after deformation are shown in Fig. 3, where R_0 and h_0 are the radius and height of the specimens before hot compression, respectively, and R_m and h are the radius and height after compression, respectively. After hot deformation, the specimens were mechanically polished and etched with the HCl(2 ml) + C_2H_5OH(96 ml) + $FeCl_3$(4 g) solution for microstructure observations.

3. Results and Discussion

3.1 Flow Stress Behavior

True stress–strain curves of the Cu-0.8 Mg and Cu-0.8 Mg-0.15 Ce alloys under different hot deformation conditions are shown in Fig. 4. Figure 4 shows that the flow stress increases with increasing strain rate and decreasing hot deformation temperature. At the initial stage of deformation, the flow stress increases rapidly with deformation. After the initial increase, the flow stress stabilizes and in some cases decreases slightly after reaching a peak value. It is well known that the hot

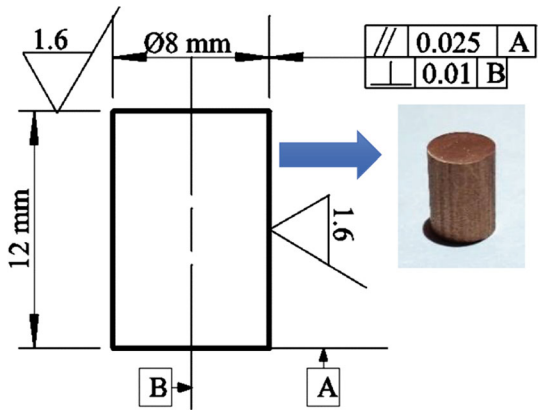

Fig. 1 Dimensions of the tested specimens for mechanical processing maps

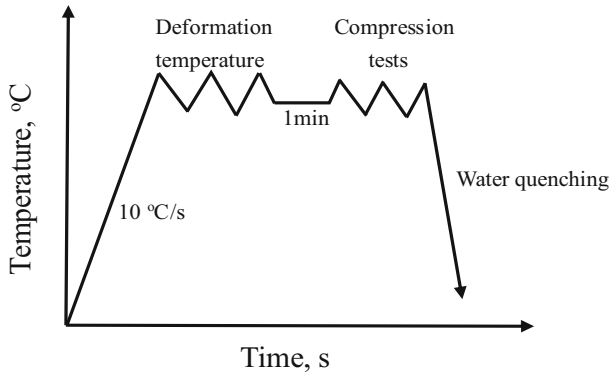

Fig. 2 Schematics of the temperature profile for hot deformation of the specimens

deformation process is affected by work hardening and dynamic softening (Ref 16). At the initial stage of deformation, a large amount of lattice distortion occurs in the crystal, and many dislocations are generated in the material. Higher dislocation density increases the probability of dislocation entanglement, thus increasing the resistance of dislocations to move, resulting in work-hardening behavior. With the continuous movement and rearrangement of dislocations, the diffusion of vacancies in the crystal, the thermal activation, dynamic recovery and recrystallization occur in the alloy, which all alter the flow stress of the alloy (Ref 17, 18). The flow stress increases to a peak value rapidly and then begins to decrease until it reaches a relatively steady value, which is shown at a deformation temperature of 500°C in Fig. 4(a) and (b). It can also be seen that dynamic recovery occurs at 500°C in Fig. 4(c) and (d). The flow stress at this stage of deformation rapidly increases because of the work hardening. Then, a balance between work hardening and dynamic recovery is reached.

It is clear that the flow stress of the Cu-0.8 Mg-0.15 Ce alloy is higher than the Cu-0.8 Mg alloy. At 0.3 true strain, 0.001 s^{-1} strain rate and 500°C deformation temperature, the flow stress of the two alloys is 149 MPa and 165 MPa, respectively. The reason is because the Ce addition restricts the movement of dislocations.

3.2 Effect of Ce Addition on Hot Deformation Parameters

Table 1 and 2 shows the peak stress of the Cu-0.8 Mg and Cu-0.8 Mg-0.15 alloys under different hot deformation conditions, respectively. The relationship between the strain rate, temperature and the flow stress of the Cu-0.8 Mg-0.15 Ce alloy can be described by the Arrhenius equation (Ref 19–23). Here, $\dot{\varepsilon}$ is the strain rate (s^{-1}), σ is the peak stress (MPa), Q is the activation energy of deformation (kJ mol^{-1}), R is the universal gas constant (8.314 kJ mol^{-1} K^{-1}), T is the temperature (K) and A, n, and α are materials constants. $\ln\sigma - \ln\dot{\varepsilon}$ and $\sigma - \ln\dot{\varepsilon}$ diagrams of the Cu-0.8 Mg-0.15 Ce alloy are drawn by the least squares linear regression, as shown in Fig. 5. The value of α is calculated to be 0.009 MPa^{-1}.

Assuming that the value of Q does not vary with the change of deformation temperature in the calculation process, Eq. (1) can be written as:

$$\dot{\varepsilon} = A[\sinh(\alpha\sigma)]^n \exp\left[-\frac{Q}{RT}\right] \quad \text{(Eq 1)}$$

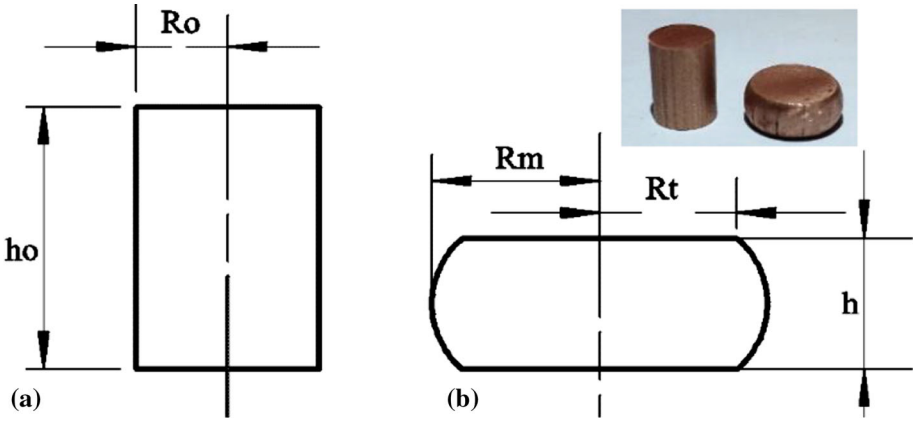

Fig. 3 Schematics of the sample geometry: (a) before compression and (b) after compression

$$\ln \dot{\varepsilon} = \ln A + n \ln[\sinh(\alpha\sigma)] - Q/RT \quad \text{(Eq 2)}$$

By taking a partial derivative of Equation (2) with respect to T, the formula for Q can be obtained:

$$Q = R \frac{\partial \ln \dot{\varepsilon}}{\partial \ln[\sinh(\alpha\sigma)]}\bigg|_T \frac{\partial \ln[\sinh(\alpha\sigma)]}{\partial\left(1/T\right)}\bigg|_{\dot{\varepsilon}} \quad \text{(Eq 3)}$$

Figure 6 shows the scatter plots and the linear regression fits for the Cu-0.8 Mg-0.15 Ce alloy. The average slopes of five straight lines can be calculated from Fig. 6(a) and (b). The corresponding n in Eq. (2) is $\frac{\partial \ln \dot{\varepsilon}}{\partial \ln[\sinh(\alpha\sigma)]}\Big|_T$, and the S value in $Q = RnS$ is $\frac{\partial \ln[\sinh(\alpha\sigma)]}{\partial(1/T)}\Big|_{\dot{\varepsilon}}$ in Eq. (3). The calculations are performed with the following values: n = 6.34, S = 5.34, and Q = 281.47 kJ mol^{-1}.

Many studies have shown that the following relations exist between the Zenner parameter Z, stress, temperature and so on (Ref 24, 25). Taking natural logarithms of both sides of Eq. (4) yields:

$$Z = \dot{\varepsilon} \exp\left(Q/RT\right) = A[\sinh(\alpha\sigma)]^n \quad \text{(Eq 4)}$$

$$\ln Z = \ln A + n \ln[\sinh(\alpha\sigma)] \quad \text{(Eq 5)}$$

According to the relationship between lnZ and ln[sinh($\alpha\sigma$)], scatter plots of lnZ and ln[sinh($\alpha\sigma$)] are drawn and a linear fit is shown in Fig. 7. The intercept after linear fitting represents the value of ln$A$, and $A = e^{31.6}$.

Finally, the values of various parameters sought are substituted into Eq. (1), and the constitutive equation for the Cu-0.8 Mg-0.15 Ce alloy suitable for hot working process analysis is:

$$\dot{\varepsilon} = e^{31.6}[\sinh(0.09\sigma)]^{6.34} \exp\left[-\frac{281.47}{RT}\right] \quad \text{(Eq 6)}$$

Using the above calculation method, one can also conclude that the constitutive equation for the Cu-Mg alloy suitable for hot working process analysis is:

$$\dot{\varepsilon} = e^{18.8}[\sinh(0.09\sigma)]^{5.40} \exp\left[-\frac{177.88}{RT}\right] \quad \text{(Eq 7)}$$

Calculated deformation activation energy of the Cu-0.8 Mg alloy is 177.88 kJ mol^{-1}, and 281.47 kJ mol^{-1} for the Cu-0.8 Mg-0.15 Ce alloy, based on the constitutive equations of the two alloys. Therefore, the trace addition of Ce increases the hot deformation activation energy of the Cu-0.8 Mg alloy. The reason is that the addition of Ce refines grains and hinders the movement of dislocations; thus, the thermal stability of the alloy is improved.

3.3 Processing Maps of the Cu-0.8 Mg and Cu-0.8 Mg-0.15 Ce Alloys

The processing map is a graph drawn based on the dynamic model of material behavior during plastic deformation processing. It directly reflects the changes of material microstructure under different processing conditions (deformation temperature and deformation rate). On the one hand, it predicts the quality of metal hot working. On the other hand, it provides guidance for selection of plastic deformation parameters (Ref 26–28).

Per unit time and volume, the total external energy absorbed by the material is P. P consists of the two dissipative quantities, J and G. The J energy is used for microstructure transformation, and the G energy is used for plastic deformation. The corresponding mathematical expression is (Ref 29, 30):

$$P = \sigma \cdot \dot{\varepsilon} = G + J = \int_0^{\dot{\varepsilon}} \sigma \mathrm{d}\dot{\varepsilon} + \int_0^{\sigma} \dot{\varepsilon} \mathrm{d}\sigma \quad \text{(Eq 8)}$$

Here, σ is the test stress (MPa), $\dot{\varepsilon}$ is the test deformation rate (s^{-1}), G is the power dissipation during plastic deformation (kJ), and J is microstructure-related power dissipation during deformation (kJ).

The amount of energy consumed in the process of microstructure transformation is determined by the sensitivity factor m:

$$m = \frac{dJ}{dG} = \frac{\dot{\varepsilon} d\sigma}{\sigma d\dot{\varepsilon}} = \frac{d \ln \sigma}{d \ln \dot{\varepsilon}} \quad \text{(Eq 9)}$$

The power dissipation coefficient η is re-introduced to represent the ratio of the dissipation covariance to the total dissipation covariance under any condition during hot working. The higher the power dissipation coefficient, the better the processing performance:

$$\eta = \frac{J}{J_{\max}} = \frac{2m}{m+1} \times 100\% \quad \text{(Eq 10)}$$

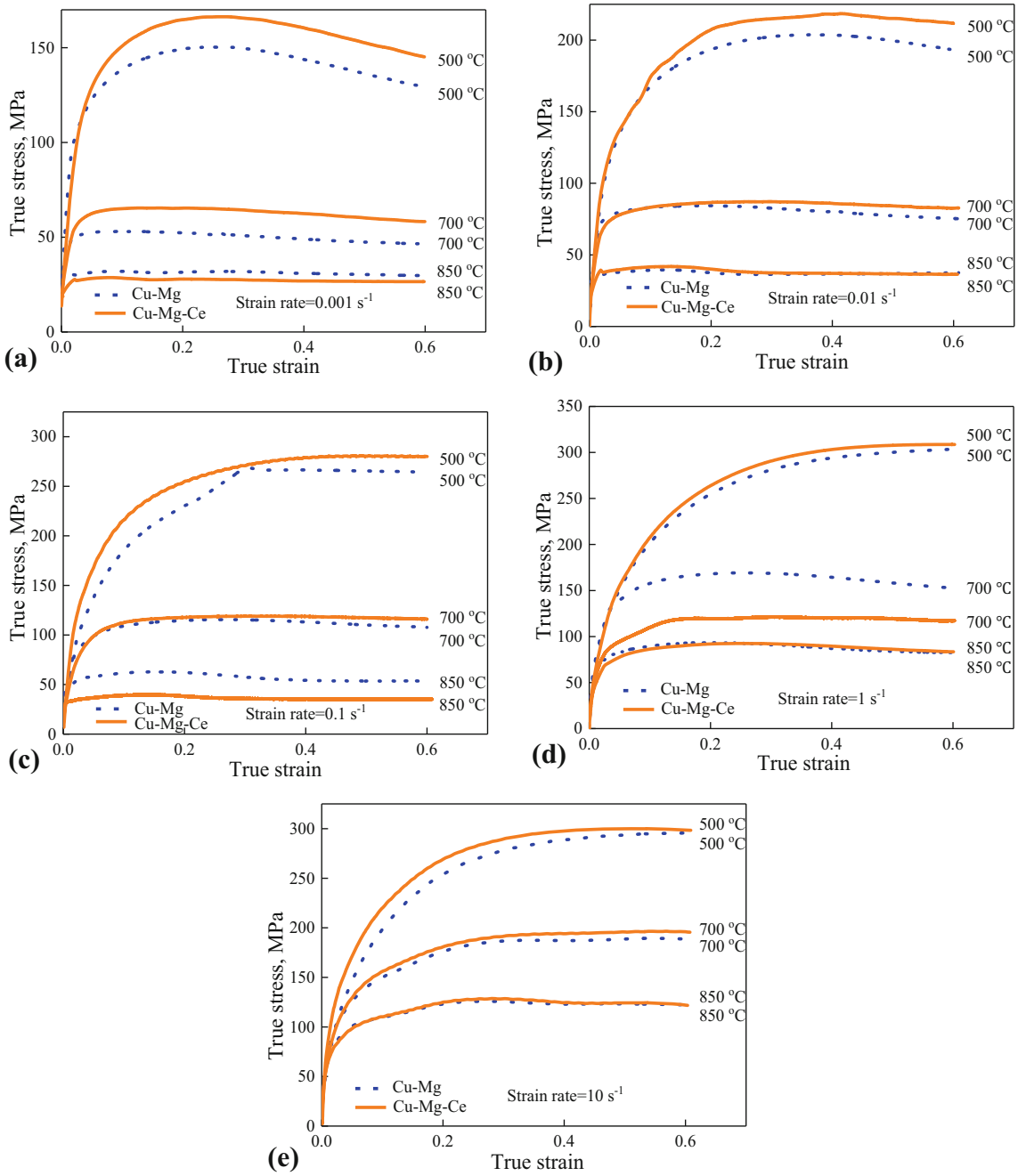

Fig. 4 True stress–strain curves of the Cu-0.8 Mg and Cu-0.8 Mg-0.15 Ce alloys under different hot deformation conditions

Table 1 Peak stress of the Cu-0.8 Mg alloy under different hot deformation conditions

	Strain rate, s^{-1}				
Deformation temperature, °C	**0.001**	**0.01**	**0.1**	**1**	**10**
500	160.40	203.77	250.26	290.68	318.87
600	92.82	133.19	180.91	227.48	264.89
700	53.12	84.39	115.59	160.18	189.36
800	30.58	53.84	78.72	108.77	143.17
850	24.01	39.52	65.92	93.46	120.94

The non-dimensional parameter ξ is commonly used to describe the rheological instability of materials at a certain deformation temperature and a certain deformation rate:

$$\xi(\dot{\varepsilon}) = \frac{\partial \ln[m/(m+1)]}{\partial \ln \dot{\varepsilon}} + m < 0 \quad \text{(Eq 11)}$$

Table 2 Peak stress of the Cu-0.8 Mg-0.15 Ce alloy under different thermal deformation conditions

	Strain rate, s^{-1}				
Deformation temperature, °C	**0.001**	**0.01**	**0.1**	**1**	**10**
500	178.33	218.47	260.70	294.65	317.16
600	113.86	150.80	187.00	218.40	248.50
700	60.44	87.18	116.99	145.83	179.54
800	35.31	58.37	84.92	113.11	145.70
850	22.72	38.88	57.47	80.53	105.71

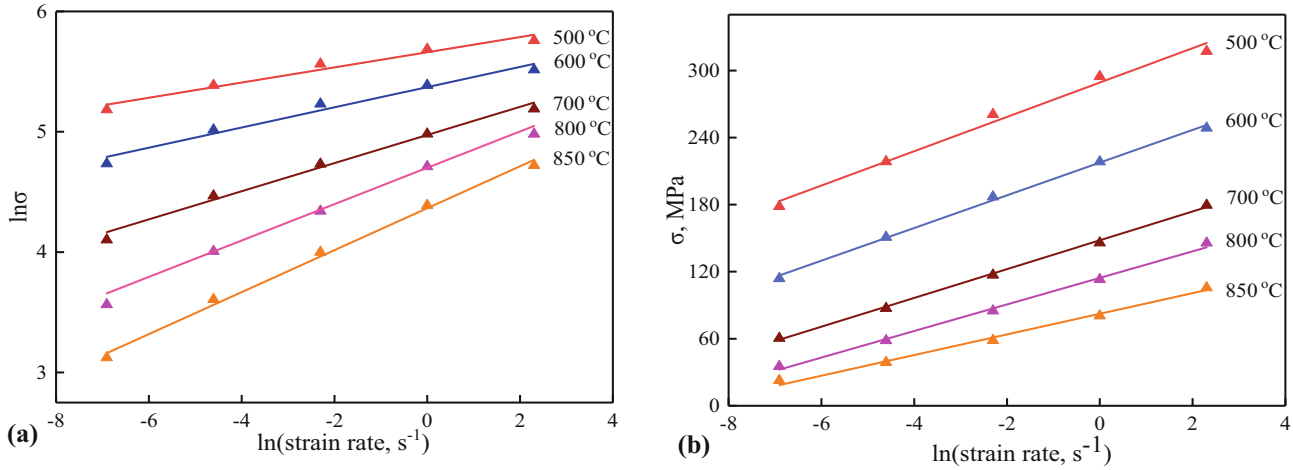

Fig. 5 Relationship between the strain rate and the stress for the Cu-0.8 Mg-0.15 Ce alloy at different temperatures

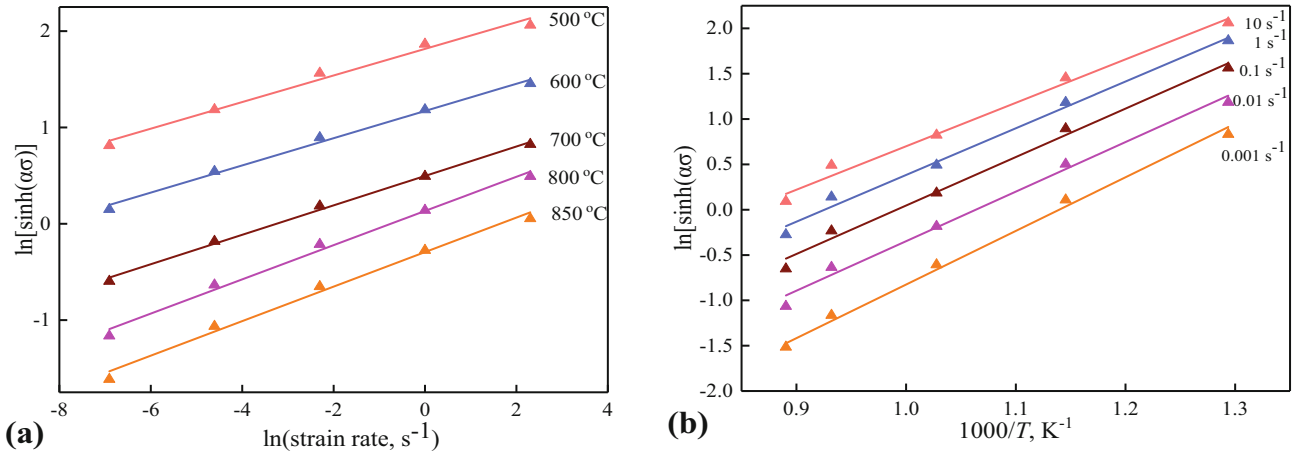

Fig. 6 Relationship between (a) $\ln[\sinh(\alpha\sigma)]$ and $\ln\dot{\varepsilon}$; (b) $\ln[\sinh(\alpha\sigma)]$ and $1000/T$ for the Cu-0.8 Mg-0.15 Ce alloy

Thermal deformation of material satisfying Eq. (10) will result in rheological instability, which must be avoided during hot working. An instability diagram can clearly describe the unstable region of the microstructure in the hot working process of materials. The contour diagram with deformation temperature and deformation rate as variables is used as the rheological instability diagram of materials (Ref 31, 32). The processing maps are obtained by superimposing the power dissipation diagram and the rheological instability diagram.

Table 3 and 4 shows the stress and strain of the Cu-0.8 Mg and Cu-0.8 Mg-0.15 Ce alloys under different hot deformation conditions, respectively. Figure 8 and 9 shows the processing maps and 3D surfaces of the $\xi(\dot{\varepsilon})$ value of the Cu-0.8 Mg and Cu-0.8 Mg-0.15 Ce alloys with a true strain of 0.2, 0.4 and 0.55 in hot compression tests, respectively.

There are two domains in the processing maps, one is the unstable domain, which is the shadowed region, and the other is the stable domain. The curves with numerical values represent the power dissipation coefficients corresponding to different processing temperatures and deformation rates under certain strains. The larger the coefficients are, the more energy is consumed and the better the processing performance is (Ref 33). Therefore, the region with large dissipation coefficient

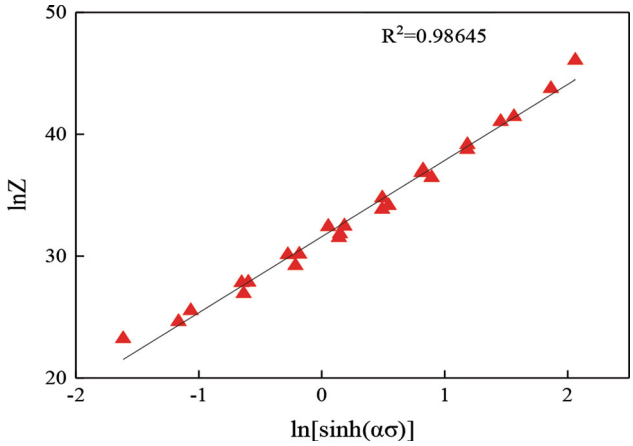

Fig. 7 Relationship between lnZ and ln[sinh(ασ)] for the Cu-0.8 Mg-0.15 Ce alloy

should be selected while avoiding the rheological instability zone when the processing parameters are determined. As shown in Fig. 8 and 9, the distribution characteristics of the energy dissipation are similar, which increase with temperature and strain rate. The unstable regions were obviously affected by the strain, and the unstable regions' area increases with strain. The black box area in the hot working drawing is the best processing area for the alloy in the hot working process.

Figure 8 shows that the optimal processing of the Cu-0.8 Mg alloy is achieved with the deformation temperature of 700-800°C and the strain rate of 0.01-0.1 s^{-1}. When the strain is 0.4, optimal processing is achieved with the deformation temperature of 650-800°C and the strain rate of 0.001-0.1 s^{-1}. When the strain is 0.55, optimal processing is achieved with the deformation temperature of 650-800°C and the strain rate of 0.001-0.1 s^{-1}.

Figure 9 shows that optimal processing of the Cu-0.8 Mg-0.15 Ce alloy is achieved with the deformation temperature of

Table 3 Stress of the Cu-0.8 Mg alloy under different hot deformation conditions and strains

		Strain rate, s^{-1}				
True strain, %	Deformation temperature, °C	0.001	0.01	0.1	1	10
20	500	149.31	193.38	230.18	254.53	254.16
	600	89.21	129.51	179.35	210.36	232.52
	700	52.30	84.36	114.70	168.13	176.31
	800	36.92	50.74	75.33	108.16	139.02
	850	31.52	37.47	61.98	93.45	123.20
40	500	143.79	203.49	266.39	293.95	288.88
	600	81.02	125.60	185.51	231.95	252.13
	700	48.97	80.43	113.04	164.39	187.09
	800	35.86	47.51	69.36	105.64	141.30
	850	30.94	36.67	54.31	87.04	123.00
55	500	132.58	196.32	264.93	301.98	295.28
	600	75.58	118.48	180.93	233.23	254.79
	700	47.00	76.26	108.84	155.31	189.35
	800	35.38	46.54	67.29	101.26	141.36
	850	29.98	37.19	53.52	83.07	122.83

Table 4 Stress of the Cu-0.8 Mg-0.15 Ce alloy under different deformation conditions and strains

		Strain rate, s^{-1}				
True strain, %	Deformation temperature, °C	0.001	0.01	0.1	1	10
20	500	160.47	218.08	278.99	303.15	297.60
	600	98.34	143.16	198.31	235.05	225.50
	700	62.45	85.95	118.70	119.86	193.99
	800	38.29	49.21	70.79	109.21	146.16
	850	26.92	37.09	35.22	89.54	124.48
40	500	160.47	218.08	278.99	303.15	297.60
	600	98.34	143.16	198.31	235.05	225.50
	700	62.45	85.95	118.70	119.86	193.99
	800	38.29	49.21	70.79	109.21	146.16
	850	26.92	37.09	35.22	89.54	124.48
55	500	149.04	213.46	280.05	308.48	299.57
	600	90.82	135.69	195.57	237.35	225.98
	700	59.19	83.09	116.69	117.98	196.24
	800	37.14	46.93	67.51	104.85	146.86
	850	26.58	36.52	35.18	84.75	123.80

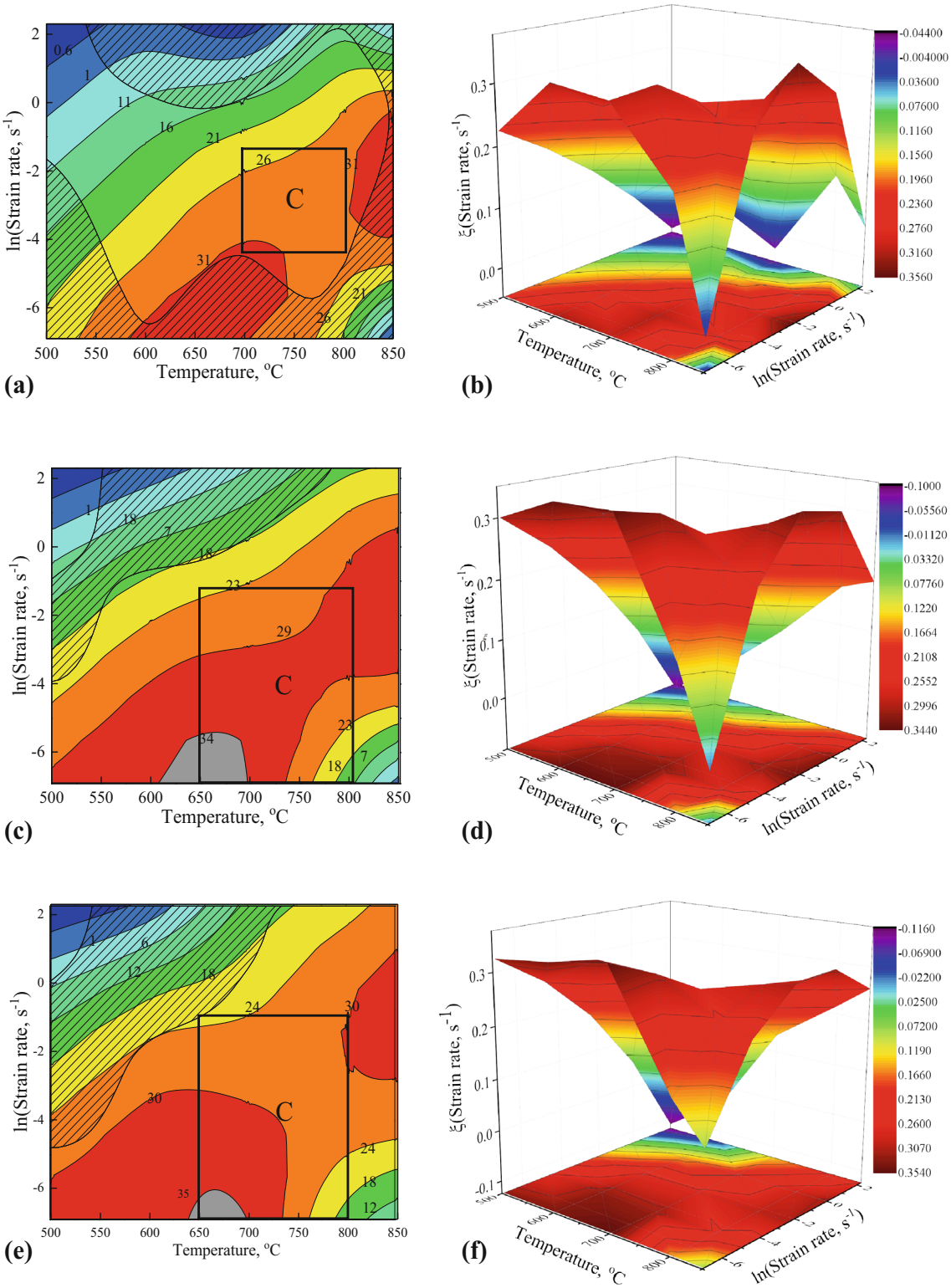

Fig. 8 Processing maps and 3D surfaces of the $\xi(\dot{\varepsilon})$ value for the Cu-0.8 Mg alloy at different strains: (a), (b) 0.2; (c), (d) 0.4; and (e), (f) 0.55

650-850°C and the strain rate of 0.001-1 s^{-1}. When the strain is 0.4, optimal processing is achieved with the deformation temperature of 650-850°C and the strain rate of 0.01-2.25 s^{-1}. When the strain is 0.55, optimal processing is achieved with the deformation temperature of 650-850°C and the strain rate of 0.01-4.48 s^{-1}.

It can be deduced from Fig. 8 and 9 that the optimal hot working parameters of the Cu-0.8 Mg alloy are the deformation temperature of 700-800°C and the strain rate of 0.01-0.1 s^{-1}, while that of the Cu-0.8 Mg-0.15 Ce alloy are the deformation temperature of 650-850°C and the strain rate of 0.01-1 s^{-1}. It is obvious that the addition of Ce enlarges the hot working area of the Cu-0.8 Mg alloy.

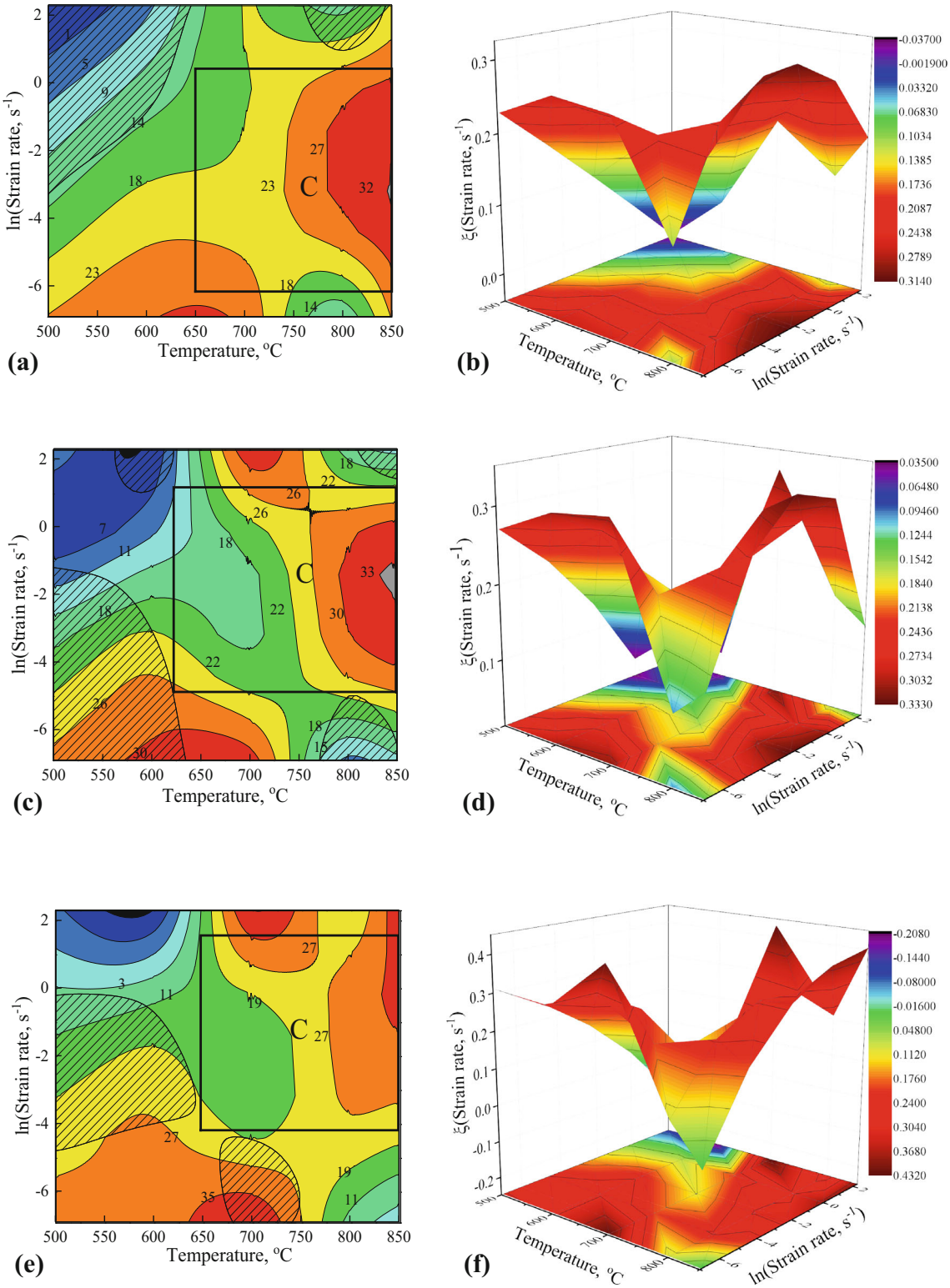

Fig. 9 Processing maps and 3D surfaces of the $\xi(\dot{\varepsilon})$ value for the Cu-0.8 Mg-0.15 Ce alloy at different strains: (a), (b) 0.2; (c), (d) 0.4; and (e), (f) 0.55

3.4 Microstructure Analysis

Figure 10 shows the x-ray diffraction pattern of the Cu-0.8 Mg and Cu-0.8 Mg-0.15 Ce alloys. Figure 10 shows that the addition of Ce promotes the precipitation of $CuMg_2$. At the same time, $CeCu_6$ and CeCu phases are generated. The generation of precipitates makes it more difficult for the movement of dislocations.

Figure 11 shows microstructure of the two alloys at different deformation conditions. Figure 11(a) shows the microstructure of the Cu-0.8 Mg alloy at the deformation temperature of 500°C and the deformation rate of 10 s^{-1}. It can be seen that

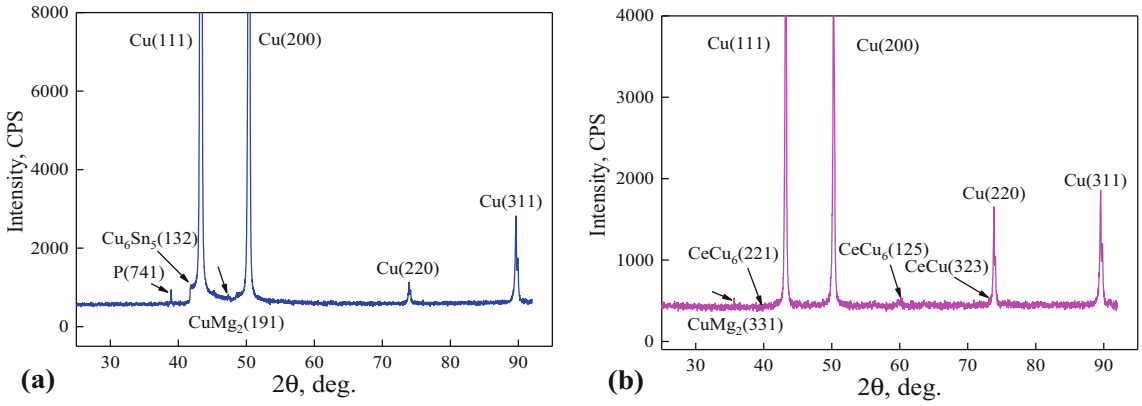

Fig. 10 XRD pattern of: (a) the Cu-0.8 Mg and (b) and the Cu-0.8 Mg-0.15 Ce alloys

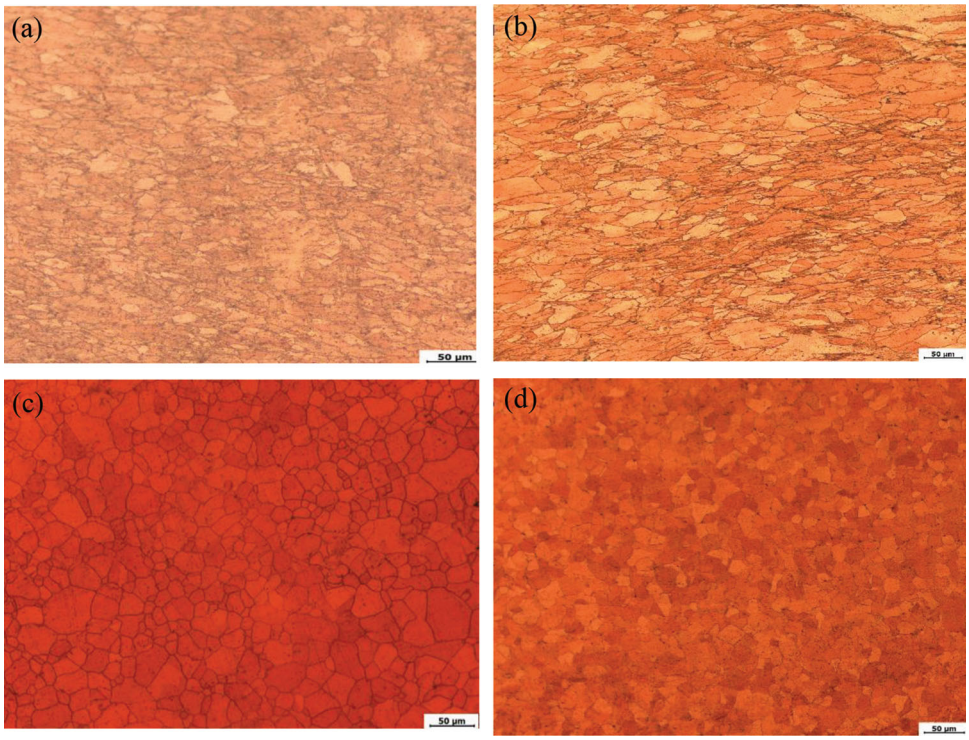

Fig. 11 Microstructure of the (a), (c) Cu-0.8 Mg and (b), (d) Cu-0.8 Mg-0.15 Ce alloys at different deformation conditions: (a) 500°C and 10 s^{-1}; (b) 500°C and 10 s^{-1}; (c) 850°C and 10 s^{-1}; and (d) 850°C and 10 s^{-1}

the alloy exhibits flattened grains due to extrusion during hot deformation in this condition. The existence of flat and long grains will cause plastic deformation of the alloy due to excessive local temperature during hot deformation (Ref 34). At high deformation rate and temperature, dynamic recrystallization is suppressed, causing plastic deformation retention. When the plasticity is poor, the material cracks easily in the hot working process, which corresponds to the unstable region in the hot processing map. At the grain boundaries of flat grains, due to the extrusion and accumulation of dislocations, the angular grain boundaries, the increase in dislocation density and the storage of many dislocations, distortion energy appears at the grain boundaries (Ref 35–38). It is easy to nucleate at the grain boundary in the Cu-0.8 Mg alloy, but because of the low deformation temperature, the atomic diffusion is affected, which hinders the occurrence of dynamic recrystallization and the growth of grains. Figure 11(b) shows microstructure of the Cu-0.8 Mg-0.15 Ce alloy at the deformation temperature of 500°C and the deformation rate of 10 s^{-1}. The alloy also exhibits flattened grains due to extrusion during hot deformation in this condition. Compared with Fig. 11(a), smaller grains are found at the grain boundaries of the elongated grains of the Cu-0.8 Mg-0.15 Ce alloy at the same conditions, indicating that dynamic recrystallization has occurred. Figure 11(c) shows the microstructure of the Cu-0.8 Mg alloy at the deformation temperature of 850°C and the deformation rate of 10 s^{-1}. There are many equiaxed grains distributed in the alloy, and complete dynamic recrystallization occurs. Figure 11(d) shows the microstructure of the Cu-0.8 Mg-0.15 Ce alloy at the deformation temperature of 850°C and the deformation rate of

10 s^{-1}. From Fig. 11(d), one can find that there are also many homogeneous fine grains inside the Cu-0.8 Mg-0.15 Ce alloy, indicating that dynamic recrystallization completed. Compared with Fig. 11(c), the grain size of the Cu-0.8 Mg-0.15 Ce alloy is smaller at the same conditions.

Based on the above analysis, it can be concluded that trace Ce addition promotes dynamic recrystallization during hot deformation. The finer the grains are, the greater the resistance of dislocations motion, thus improving the thermal stability of the alloy.

4. Conclusions

Hot deformation tests of the Cu-0.8 Mg and Cu-0.8 Mg-0.15 Ce alloys were carried out using a Gleeble-1500D thermal simulator under different deformation conditions. Based on the calculations and analysis of the experimental results, the following conclusions can be drawn:

1. The hot deformation process of the Cu-0.8 Mg and Cu-0.8 Mg-0.15 Ce alloys is affected by the work hardening and dynamic softening. Dynamic recrystallization is the main softening mechanism. The trace addition of Ce hinders the movement of dislocations in the Cu-0.8 Mg alloy, thus increasing the flow stress of the alloy during hot working.
2. The deformation activation energy of the Cu-0.8 Mg alloy is 177.88 kJ mol^{-1}, and the Cu-0.8 Mg-0.15 Ce alloy is 281.47 kJ mol^{-1}. The addition of Ce increases the hot deformation activation energy of the Cu-0.8 Mg alloy, thus improving the thermal stability of the alloy.
3. The optimal hot working parameters of the Cu-0.8 Mg alloy are deformation temperature of 700-800°C and strain rate of 0.01-0.1 s^{-1}. The optimal hot working parameters of the Cu-0.8 Mg-0.15 Ce alloy are deformation temperature of 650-850°C and strain rate of 0.01-1 s^{-1}. The addition of Ce enlarges the hot working area of the Cu-0.8 Mg alloy.
4. The microstructure is strongly affected by the deformation temperature and the strain rate. Trace Ce addition refines grains during hot deformation.

Acknowledgments

This work was supported by the National Natural Science Fund of China (U1704143) and the Science and Technology Open-Cooperate Fund of the Henan Province (182106000018). Prof. Zhou Xudong provided help with the experiments. The authors thank Vladislav Yakubov for proofreading the paper.

References

1. C.D. Xia, Y.L. Jia, W. Zhang, Q.Y. Dong, G.Y. Xu, and M. Wang, Study of Deformation and Aging Behaviors of a Hot Rolled-Quenched Cu-Cr-Zr-Mg-Si Alloy During Thermomechanical Treatments, *Mater. Des.*, 2012, **39**, p 404–409
2. Y. Pang, C.D. Xia, M.P. Wang, Z. Li, Z. Xiao, H.G. Wei, X.F. Sheng, Y.L. Jia, and C. Chen, Effects of Zr and (Ni, Si) Additions on Properties and Microstructure of Cu-Cr Alloy, *J. Alloys Compd.*, 2014, **786**, p 582
3. J.H. Su, Q.M. Dong, P. Liu, H.J. Li, and B.X. Kang, Research on Aging Precipitation in a Cu-Cr-Zr-Mg Alloy, *Master. Sci. Eng. A*, 2005, **392**, p 422–426
4. P. Liu, B.X. Kang, X.G. Cao, J.L. Huang, B. Yen, and H.C. Gu, Aging Precipitation and Recrystallization of Rapidly Solidified Cu-Cr-Zr-Mg Alloy, *Mater. Sci. Eng., A*, 1999, **265**, p 262–267
5. D.P. Lu, J. Wang, W.J. Zeng, Y. Liu, L. Lu, and B.D. Sun, Study on High-Strength and High-Conductivity Cu-Fe-P Alloys, *Mater. Sci. Eng. A*, 2006, **421**, p 254–259
6. H. Zhang, H.G. Zhang, and L.X. Li, Hot Deformation Behavior of Cu-Fe-P Alloys During Compression at Elevated Temperatures, *J. Mater. Eng. Perform.*, 2009, **209**(6), p 2892–2896
7. R. Monzen and C. Watanabe, Microstructure and Mechanical Properties of Cu-Ni-Si Alloys, *Mater. Sci. Eng. A*, 2008, **483–484**, p 117–119
8. D.M. Zhao, Q.M. Dong, P. Liu, B.X. Kang, J.L. Huang, and Z.H. Jin, Aging Behavior of Cu-Ni-Si Alloy, *Mater. Sci. Eng. A*, 2003, **361**(1–2), p 93–99
9. G.B. Lin, Z.D. Wang, M.K. Zhang, H. Zhang, and M. Zhao, Heat Treatment Method for Making High Strength and Conductivity Cu-Cr-Zr Alloy, *Mater. Sci. Technol.*, 2011, **6**(1), p 966–969
10. R. Mishnev, I. Shakhova, A. Belyakov, and R. Kaibyshev, Deformation Microstructures Strengthening Mechanisms and Electrical Conductivity in a Cu-Cr-Zr Alloy, *Mater. Sci. Technol.*, 2015, **629**, p 29–40
11. A. Kumar, P. Dhekne, A.K. Swarnakar, and M.K. Chopkar, Analysis of Si Addition on Phase Formation in AlCoCrCuFeNiSix High Entropy Alloys, *Mater. Lett.*, 2017, **188**, p 73–76
12. J. Chen, Z. Chen, H. Yan, F. Zhang, and K. Liao, Effects of Sn Addition on Microstructure and Mechanical Properties of Mg-Zn-Al Alloys, *J. Alloys Compd*, 2008, **461**(1–2), p 209–215
13. D.H. Xiao, J.N. Wang, D.Y. Ding, and H.L. Yang, Effect of Rare Earth Ce Addition on the Microstructure and Mechanical Properties of an Al-Cu-Mg-Ag Alloy, *J. Alloys Compd.*, 2003, **352**(1–2), p 84–88
14. L. Zhong, J. Peng, M. Li, Y. Wang, Y. Lu, and F. Fan, Effect of Ce Addition on the Microstructure, Thermal Conductivity and Mechanical Properties of Mg-0.5Mn Alloys, *J. Alloys Compd.*, 2016, **661**, p 402–410
15. Y. Zhang, A.A. Volinsky, H.T. Tian, Z. Chai, P. Liu, and B.H. Tian, Effects of Ce Addition on High Temperature Deformation Behavior of Cu-Cr-Zr Alloys, *J. Mater. Eng. Perform.*, 2015, **24**(10), p 3783–3788
16. H. Wu, S.P. Wen, H. Huang, X.L. Wu, and K.Y. Gao, Hot Deformation Behavior and Constitutive Equation of a New Type Al-Zn-Mg-Er-Zr Alloy During Isothermal Compression, *Mater. Sci. Eng. A*, 2016, **651**, p 415–424
17. Y.Q. Ning, X. Luo, H.Q. Liang, H.Z. Guo, and J.L. Zhang, Study of Dynamic Recrystallization in a Ni-Based Superalloy by Experiments and Cellular Automaton Model, *Mater. Sci. Eng. A*, 2015, **625**, p 432–440
18. X.M. Chen, Y.C. Lin, D.X. Wen, J.L. Zhang, and M. He, Dynamic Recrystallization Behavior of a Typical Nickel-Based Superalloy During Hot Deformation, *Mater. Des.*, 2014, **57**, p 568–577
19. S. Arrhenius, Über die reaktionsgeschwindigkeit bei der inversion von rohrzucker durch säuren, *Z. Phys. Chem.*, 1889, **4**, p 226
20. C. Zener and J.H. Hollomon, Effects of Strain Rate Upon Plastic Flow of Steel, *J. Appl. Phys.*, 1944, **15**, p 22–32
21. H.L. Sun, Y. Zhang, A.A. Volinsky, B.J. Wang, B.H. Tian, K.X. Song, Z. Chai, and Y. Liu, Effects of Ag Addition on Hot Deformation Behavior of Cu-Ni-Si Alloys, *Adv. Eng. Mater.*, 2017, **19**, p 38–46
22. B.J. Wang, Y. Zhang, B.H. Tian, J.C. An, A.A. Volinsky, H.L. Sun, Y. Liu, and K.X. Song, Effects of Ce Addition on the Cu-Mg-Fe Alloy Hot Deformation Behavior, *Vacuum*, 2018, **155**, p 594–603
23. Y. Zhang, H.L. Sun, A.A. Volinsky, B.H. Tian, K.X. Song, and Y. Liu, Hot Workability and Constitutive Model of the Cu-Zr-Nd Alloy, *Vacuum*, 2017, **146**(12), p 35–43
24. F. Chen, G. Feng, and Z. Cui, New Constitutive Model for Hot Working, *Metall. Mater. Trans. A*, 2016, **47**, p 1229–1239
25. A. Mirzaei, A. Zarei-Hanzaki, N. Haghdadi, and A. Marandi, Constitutive Description of High Temperature Flow Behavior of Sanicro-28 Super-Austenitic Stainless Steel, *Mater. Sci. Eng. A*, 2014, **589**, p 76–82
26. T. Xi, C. Yang, M.B. Shahzad, and K. Yang, Study of the Processing Map and Hot Deformation Behavior of a Cu-Bearing 317LN Austenitic Stainless Steel, *Mater. Des.*, 2015, **87**, p 303–312

27. Y. Song, P. Chang, Q. Li, L. Xie, and S. Zhu, Hot Deformation Characteristics and Processing Map of Nickel-Based C276 Superalloy, *J. Alloys Compd.*, 2015, **625**, p 738–744
28. C. Zhang, L. Zhang, W. Shen, Q. Xu, and Y. Cui, The Processing Map and Microstructure Evolution of Ni-Cr-Mo-Based C276 Superalloy During Hot Compression, *J. Alloys Compd.*, 2017, **728**, p 1269–1278
29. O. Sivakesavam and Y. Prasad, Characteristics of Super Plasticity Domain in the Processing Map for Hot Working of As-Cast Mg-11.5Li-1.5 Al Alloy, *Mater. Sci. Eng. A*, 2002, **323**, p 270–277
30. H.Z. Li, H.J. Wang, X.P. Liang, H.T. Liu, and Y. Liu, Hot Deformation and Processing Map of 2519A Aluminum Alloy, *Mater. Sci. Eng. A*, 2011, **528**, p 1548–1552
31. S.K. Oh, K.K. Lee, Y.S. Na, C.H. Suh, and Y.C. Jung, Optimization of the Hot Workability for an Extrude AZ80 Mg Alloy Using the Processing Map and Kriging Meta-Model, *Int. J. Precis. Eng. Manuf.*, 2015, **16**, p 1149–1156
32. J. Yan, Q.L. Pan, B. Li, Z.Q. Huang, Z.M. Liu, and Z.M. Yin, Research on the Hot Deformation Behavior of Al-6.2Zn-0.70 Mg-0.3Mn-0.17Zr Alloy Using Processing Map, *J. Alloys Compd.*, 2015, **632**, p 549–557
33. M. Sarebanzadeh, R. Mahmudi, and R. Roumina, Constitutive Analysis and Processing Map of an Extruded Mg-3Gd-1Zn Alloy Under Hot Shear Deformation, *Mater. Sci. Eng. A*, 2015, **637**, p 155–161
34. F.R. Castro-Fernandez and C.M. Sellars, Changes of Flow Stress and Microstructure During Hot Deformation of Al-1Mg-1Mn, *Mater. Sci. Technol.*, 2013, **6**, p 453–460
35. A.A. Hameda and L. Blaz, Microstructure of Hot-Deformed Cu-3.45 wt.% Ti Alloy, *Mater. Sci. Eng. A*, 1998, **254**, p 83–89
36. B.J. Wang, Y. Zhang, B.H. Tian, V. Yakubov, J.C. An, A.A. Volinsky, Y. Liu, K.X. Song, L.H. Li, and M. Fu, Effects of Ce and Y Addition on Microstructure Evolution and Precipitation of Cu-Mg Alloy Hot Deformation, *J. Alloys Compd.*, 2019, **781**, p 118–130
37. Y. Liu, R.L. Zhao, B.H. Tian, and X.W. Zhang, Hot-Compression Behaviors of W-50%Cu Composite, *Rare Met.*, 2011, **30**, p 610–613
38. Y. Liu, Z.Q. Yang, B.H. Tian, Y. Zhang, Z.B. Gu, and A.A. Volinsky, Hot Deformation Behavior of the 20 vol.% TiC/Cu-Al_2O_3 Composites, *J. Mater. Eng. Perform.*, 2018, **27**, p 4791–4798